Desalination and Water Treatment
www.deswater.com

doi: 10.5004/dwt.2023.29876

309 (2023) 220–235
October

A novel semi-empirical model for lifetime prediction of gravity based ceramic filter and permeability estimation

Sandeep Gupta[a], Sunil Duhan[a,*], Shubhabrata Sarkar[b], Prabhat Munshi[b], Anand Krishnan Plappally[a]

[a]*Mechanical Engineering Department, Indian Institute of Technology Jodhpur, Jodhpur 342037, India, email: sunil.2@iitj.ac.in (S. Duhan)*
[b]*Mechanical Engineering Department, Indian Institute of Technology Kanpur, Kanpur, 208016, India*

Received 5 July 2023; Accepted 28 August 2023

ABSTRACT

By reducing chemical, physical, and microbial contaminants, gravity-based ceramic water filters have proven to be a promising alternative for drinking water treatment. Acceptance of these filters, however, is contingent on a sufficient flow rate and the filtration efficiency. The lifetime and filtration efficiency of these filters depend on the active sites present at the internal surface exposed to the water in contact with the porous media and porous structure. The filtration rate of these filters is calculated using the Darcy equation. In literature semi–empirical relations are available between absolute permeability (K), porosity (φ), specific surface area (S) and Kozeny–Carmen constant (C_{kc}). Grain diameter and tortuosity can be calculated for these porous structures. In the present study, the Kozeny–Carmen constant (C_{kc}) is calculated for sintered ceramic material where the pore structure is difficult to approximate to a well-defined internal geometry. The sintered porous structure is obtained by mixing the clay material with an equal volume of sawdust in partially saturated water condition and sintered at a peak temperature of 850°C. Pore structure from the sintered material is digitally generated using micro-CT scanning at the machine resolution of 28.3 μm followed by image processing. Since sintered ceramic material exhibits pore space ranging from sub-micrometre to mm scale, low resolution scanning is used to capture the large region of interest (RoI). Digital geometries are simulated for the flow field inside the pore structure. Simulated permeability is calculated, which is compared with experimental permeability values. Results show that the permeability is a function of log normal porosity values. A correction factor (CF) is introduced and calculated for all simulated data to eliminate the error introduced in the simulated results due to the low resolution of the micro-CT scanner. From these results, an empirical relation between the permeability and porosity is determined. The predicted lifetime of a ceramic filter is based on the change in porosity caused by particle depth filtration and the corresponding pressure gradient available for gravity-based filtration at respective times during operation. Thus, a novel relationship between Kozeny–Carmen constant (C_{kc}) and porosity (φ) is proposed for predicting the lifetime of the ceramic water filter material.

Keywords: Kozeny–Carmen; Permeability; Porous media; Flow; Lifetime; Micro-CT

* Corresponding author.

Presented at the European Desalination Society Conference on Desalination for the Environment: Clean Water and Energy, Limassol, Cyprus, 22–26 May 2023

1. Introduction

Ceramic filters have emerged as sustainable and cost-effective methods for drinking water treatment in various regions worldwide. These filters utilise gravitational energy to purify water and can be further enhanced through the incorporation of additive materials to treat industrial wastewater [1]. The efficacy and efficiency of ceramic filters are contingent upon the quality of the water source and the primary raw materials employed. Furthermore, the design and structure of the filter itself can significantly impact its performance. Regular maintenance and cleaning are vital to ensuring optimal filtration efficiency. Continuous research and development in ceramic filter technology aim to enhance its effectiveness in addressing diverse water sources and contaminants [2]. Gravity-based ceramic water filters exhibit promising potential for reducing chemical, physical, and microbial contaminants in drinking water. However, their acceptance hinges on achieving adequate flow rates and filtration efficiency. Active sites present at the internal surface that come into contact with the porous media and structure have an impact on the lifespan and filtration effectiveness of these filters [3].

Evaluating the filtration rate of these filters involves employing the Darcy equation. Existing literature provides semi-empirical relationships between absolute permeability (k), porosity (φ), specific surface area (S), and the Kozeny–Carmen constant (C_{kc}). Calculating grain diameter and tortuosity is essential for characterising these porous structures [4]. This study is to find the Kozeny–Carmen constant (C_{kc}) for sintered ceramic material with a complex pore structure that can't be approximated by a well-defined internal geometry. By partially saturating a mixture of clay material and sawdust with water and sintering it at a peak temperature of 850°C, one can create the sintered porous structure. Micro-CT scanning at a resolution of 28.3 μm, followed by image processing, is employed to generate digital representations of the pore structure. Since sintered ceramic material exhibits a pore space ranging from sub-micrometre to mm scale, low-resolution scanning is utilised to capture a large region of interest (RoI) [5]. The generated digital geometries are then simulated to analyse the flow field inside the pore structure. Simulated permeability is calculated and compared with experimental permeability values, revealing that permeability is a function of lognormal porosity values [6].

To address the limitations introduced by the low resolution of the micro-CT scanner, a correction factor (CF) is introduced and computed for all simulated data, eliminating potential errors in the results. From these findings, an empirical relationship between permeability and porosity is established [7]. The predicted lifetime of a ceramic filter is determined based on the changes in porosity resulting from particle depth filtration and the corresponding pressure gradient available for gravity-based filtration during operation. Consequently, a novel relationship between the Kozeny–Carmen constant (C_{kc}) and porosity (φ) is proposed to predict the lifetime of ceramic water filter materials [8]. This proposed relationship considers the influence of particle depth filtration and gravity-based filtration on the porosity of ceramic water filter materials. By incorporating the Kozeny–Carmen constant, it provides a more accurate estimation of the filter's lifetime compared to previous models [9]. This novel approach can greatly assist in optimising the design and performance of ceramic water filters for various applications. Additionally, this proposed relationship can also help identify potential areas for improvement in the manufacturing process of ceramic water filter materials [1]. By understanding the factors that affect the porosity, manufacturers can make adjustments to enhance the durability and longevity of the filters. This research has the potential to revolutionise the field of ceramic water filtration and contribute to providing clean and safe drinking water to communities worldwide [10].

The manufacturing methods differ from location to location since clay is distinct with geography. Therefore, manufacturing may have specific processes for a specific location, and it is related to raw material availability. Ceramic gravity water filters are an important source of pure water in rural areas [11]. These filters are manufactured manually by traditional methods which takes time in the range from 10 to 20 d. These filters vary in size and shape as per the requirement of the flow rate add filtration efficacy [12]. Various additive materials can be impregnated to target the adsorption of different chemicals in order to treat the water (Ajayi et al. [13]). The present study aims at the development of frustum shaped ceramic water filters. They treat 8–10 L of water. Frustum shaped ceramic filter sits on another mesoporous ceramic vessel acting as a cooling pot. It would hold the filtered water [14].

Porous media can be described and analysed at various length scales. The structural characteristics of porous media (here frustum shaped ceramic water G-filter) and physiochemical interaction with the pore fluid are provided importance here. The scale of interest can vary from molecular level (10–11 m) to mega level (106 m) [15]. Pore-scale modelling of fluid flow can be used to predict the flow properties inside the porous media and the transport behaviour of ions present in water. Pore-scale modelling is used to calculate the permeability of G-filters numerically and compared it with the experimental data [16]. The relationship between computed permeability and experimental permeability is used to explore the relationship between two different length scale properties. Computed permeability of the whole frustum can be modelled if one knows the total structural volume of the frustum vessel of the G-filter [17]. Along with permeability and porosity, pore length can influence flow breakage, as well as adsorptive aspects should be brought here, since that is the aim of topographical image data analysis [18].

Pore-scale imaging and modelling has a potential to analyse contaminant transport and ionic transport through clay ceramic porous media. This study describes the numerical recipe to simulate flow inside the porous structure in order to study the effect of porous microstructure and clayley ceramic property on the filtration efficiency [19]. Using these simulations, permeability is computed for the G-filter and then compared to the experimental permeability. The correction factor is estimated for the simulated permeability which is generated due to the finite nature of resolution of micro-CT images [20]. This correction factor is used to map with velocity profile inside the porous structure and error free velocity profile is stimulated. Further analysis is

performed on these corrected simulated results to predict the efficiency of the clayley ceramic water filters. Also, modification in Darcy's law is suggested to overcome the error generated due to low resolution micro-CT images [20,21].

Waterborne diseases and diarrhoea pose a significant threat to human life, leading to a high number of annual fatalities and impacting approximately half a billion individuals [22]. Least developed countries face a greater risk of water contamination due to water stress and inadequate industrial and urban planning. To combat this issue, innovative technologies are being developed to mitigate water-related problems. Point-of-use (PoU) solutions, including reverse osmosis (RO), activated carbon, activated alumina, ultraviolet disinfection (UV), boiling, and ceramic filters, are prominent areas of research. Historical records trace the origins of water purification for drinking back to 2000 BC [23]. Evaluating energy consumption in water treatment techniques provides valuable insights into operational costs [14,24].

2. Ceramic filters manufacturing

Western Rajasthan potters practise traditional pottery-making techniques characterised by the manual rotation of the wheel [14]. In this region, the manufacturing procedure for clay ceramic water filter containers has not been mechanised. Raithal and Mokalsar near Jodhpur, Rajasthan, are mined for unprocessed salty clay, which is then ground into a powder. Women then sieve the clay through a domestic sieve with dimensions of 3 by 3 mm, deviating slightly from the Potter for Peace recommendation of 0.18 to 2 mm sieve sizes [14]. If the salt content of the clay declines below 0.02% by volume, additional salt is added to improve the load-bearing capacity, whiteness, and water-refrigeration properties of the clay ceramics. Local artisans believe that the inclusion of salt affects the rates of firing for clay ceramics [14]. In accordance with customary practises in Western Rajasthan, soil and organic matter, namely sawdust, are meticulously mixed to produce structurally sound building materials. The sawdust is sieved with the same sieve used for the pulverised salty clay, in accordance with the Potter for Peace-recommended method for preparing the clay-sawdust mixture for the production of filter greenware [25]. In this study, disc-shaped composites are formed by combining a homogenous mixture of sawdust and salty clay in equal volumes with water constituting 70% of the mixture by volume. The composites are left overnight under a saturated cloth cover, and then a 30-ton press from Y&Co Ltd., India is used to press-form them into frustum shapes [14]. To prevent the formed green body from adhering to the mould wall, 96-inch-diameter plastic bags are wrapped around frustum-shaped aluminium moulds [15]. It should be noted that frustum-shaped water filter presses are available in various forms and are in use around the globe (Fig. 1) of the indigenous filter press, which was designed to produce a nine-litre filter green body of the composite blend [14,26].

3. Lifetime and permeability of gravity

The longevity of gravity filters is contingent upon the density of active sites within the ceramic material. These active sites can be quantified through cation exchange capacity (CEC) experiments, providing insights into their efficacy. Furthermore, the permeability of ceramic filters is intrinsically linked to their internal structure, which dictates the flow of fluids. Empirical formulae have been developed to estimate permeability for diverse porous structures, facilitating a comprehensive understanding of filtration performance. The assessment of active site density and permeability contributes to the optimization and design of ceramic filters, enhancing their efficiency and effectiveness in water treatment applications.

3.1. Flow rate experiments

Filtration through flat porous ceramic plate (PCPs) manufactured are considered. Ceramic samples thus prepared from 50C:50S and 55C:45S compositions are named 50R and

Fig. 1. Steps of ceramic filters manufacturing.

55R, respectively sintered sample. The hydrostatic pressure distribution remains invariant in space and changes only with time which can be calculated. Flow experiment setup consists of three main components. Acrylic wall container, bottom of this container is the PCP through which the water from the container will percolate and cumulative filtrate data measurement apparatus using electronic balance (Contech Instruments, CTL-600, India) having 0.01 g accuracy. Purified water was used as pre-filtrate in the experimental water loading (UV-RO, Thermo Scientific, India). Fluid flow through these PCP samples was studied under consecutive or cyclic water loading events. During an event flow is forced to flow in perpendicular direction of the PCP sample surface. PCP samples were joint with acrylic walls using silicon sealant (Exsan® specialities Weather silicon sealant-700-nonacidic, Navi Mumbai, India) and contained 24 cm of water. The event is defined as decrease in height of water from 27 to 3 cm due to percolation through the PCP under the effect of gravity. Here the gauge pressure may vary from 0.02646 to 0.000294 bar which mimics the operating condition of filtering base surface for available ceramic filters such as Filtron. Kosim, G-filter and other disk filters [27–29].

The PCPs 50R and 55R are used for cyclic loading filtration test events. The cumulative flow rate or porous percolation rates have been plotted for individual filtration events for the respective filters in Fig. 3. Filtration rates of water at consecutive run events (denoted here as R1, R2 and R3) shows the change in flow rate which may influence timely evolution of micro-structure in the PCPs.

The initial three filtration runs performed one after the other through ceramic disk filters with equal volume fractions of sawdust and clayey soil is following the relation 50-R2 < 50-R1 < 50-R3 and 55-R2 < 55-R1 < 55-R3 [30]. This phenomenon of large flow rate in the second run is quite evident from Fig. 3.

3.2. Permeability

Pore-scale imaging and modelling techniques have significant potential for analysing contaminant transport and ionic movement within the porous media of clay ceramics. This study presents a numerical method for simulating flow behaviour within a porous structure in an effort to determine the influence of microstructural characteristics and clay ceramic properties on filtration efficacy. These simulations calculate the permeability of the G-filter, which is then compared to experimental measurements as depicted in Fig. 2. To account for the limited resolution of micro-CT images, a correction factor for the approximated permeability is determined, enabling the mapping of velocity profiles within the porous structure and producing an error-free representation. To predict the efficacy of clay ceramic water filters, the corrected simulation results are subjected to additional analysis. In addition, a proposed modification to Darcy's law addresses the defects introduced by micro-CT images with low resolution.

$$\Delta p = h_0 - h \times \rho \times g$$

Fig. 2. G-filter receptacle in a clay container (Left). G-filter receptacle in a plastic container (Right) [14].

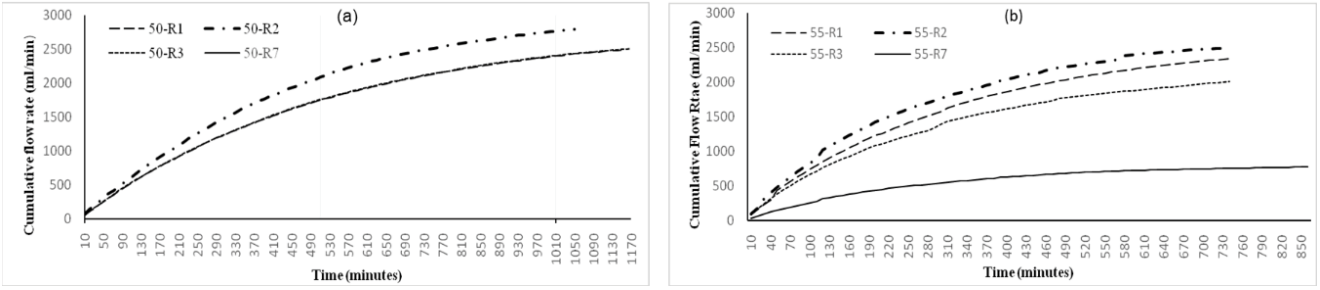

Fig. 3. Cumulative flow rate for cyclic load runs for (a) composition 50R and (b) composition 55R.

$$h = \frac{\dot{Q}}{A}$$
$$\dot{Q} = \frac{V}{t} \quad (1)$$
$$\Delta p = h_0 - \left(\frac{V\rho g}{tA}\right)$$

where, h_0 is an initial water height (= 22 cm), V is a volume of filtrate between two readings, t is a time interval, A is cross-sectional area of ceramic ware, h is a height of water head at time t, ρ is density of water at 30°C (= 1,000 kg/m^3) and g is gravitational acceleration. Fig. 4a and b along with Eq. (1) indicate the strong relation between permeability and pressure head. Fig. 4 also indicates the variation of permeability with filtration runs which can be correlated with the change in internal structure such as porosity, SNSVR and aspect ratio of ceramic plate wares. Changes in filtration rate, aspect ratio and porous surface area after each filtration event indicates permeability variation during specific filtration events [31]. The phenomenon of increase in permeability during the second run as illustrated in Fig. 3 is synonymous to the observed surge of flow during this run. The permeability values observed in Fig. 3 are at par with other experiments performed elsewhere on ceramic water filters [32]. Fig. 3 indicates the strong relation between permeability and pressure variation occurring with time.

These microstructure studies can also be extended for the study of strength behaviour of these PCPs with time duration of cyclic loading since porosity variations is found to mimic aspect ratio variation. Porosity values which are formed by using clay with some faults are obtained with micro-computed tomography (micro-CT, Procon X-Ray CT-mini, IIT Kanpur) image analysis as discussed earlier [33,34]. The surge in flow rate through the porous media can be correlated to the change in porosity as illustrated in Fig. 5. The results of permeability experiments indicate that the flow rate stabilises in the third run and then decreases in subsequent runs. This demonstrates a time-dependent change in permeability and highlights the effect of pressure differences on permeability behaviour. The implemented filter assembly has a filtration rate of approximately 0.8 L/h, which quantifies the filtration capacity. Permeability, which is the ability to fluid flow through porous material. Permeability can be estimated by equation given in Eq. (2).

$$\text{Flow rate}(Q) = \kappa \frac{A\nabla p}{\mu \Delta x} \quad (2)$$

The flow rate through porous media can be calculated using the wet area (A), pressure gradient (p), fluid viscosity (μ), and porous media thickness (Δx). In addition, the permeability value (K) can be calculated using the Kozeny–Carman equation, which establishes a relationship between the flow parameters and the inherent properties of the porous medium. By employing these equations, the flow behaviour and permeability of porous media can be precisely determined, thereby facilitating a thorough comprehension of fluid dynamics in porous systems.

$$\kappa = c \frac{\varphi^3}{(1-\varphi)^2 S_s} \quad (3)$$

where, c is constant, and it depends on the internal structure of porous media. The value of c does not include the effect of microstructure, where flow is dominated by capillary pressure. In Eq. (3) constant c can be associated with structure. Another important factor using Kozeny's–Carman equation as that value of constant c is experimentally and

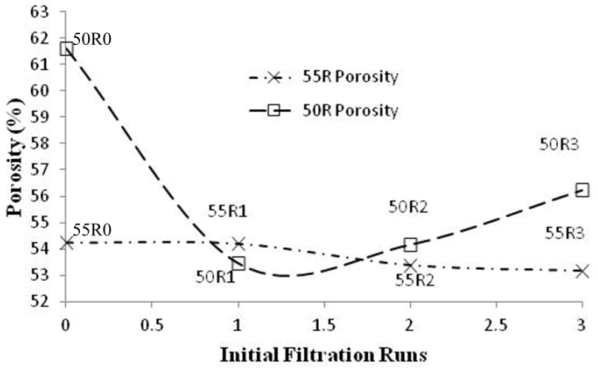

Fig. 5. Porosity variation in the 50R and 55R PCP samples under cyclic water loading events.

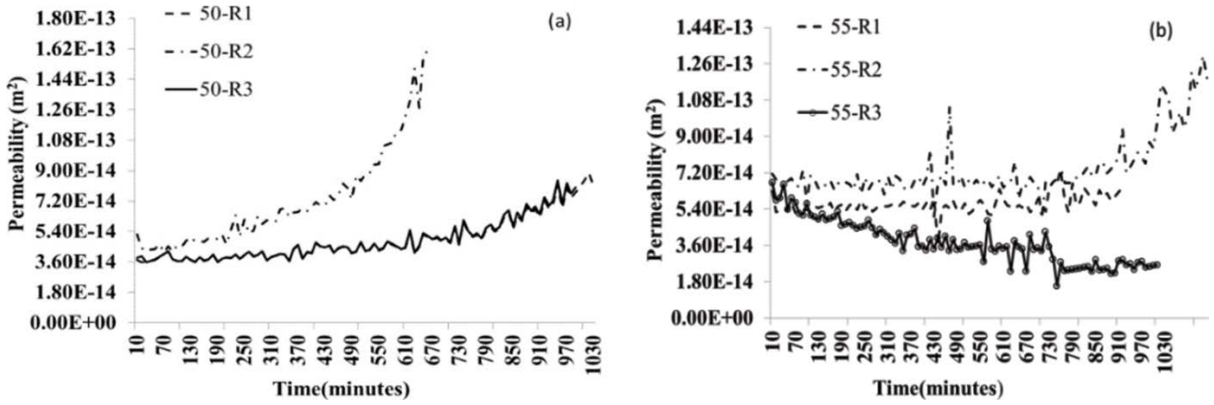

Fig. 4. Permeability variation cyclic loading events R1, R2 and R3 for (a) composition 50R and (b) composition 55R.

analytically found out assuming pore space generated by granular particles. Application of such formulation to pore space generated in microstructure in sintered ceramic material where defining grain diameter and subsequent calculation is error prone is doubtful. Estimation of specific surface area is also questionable in such micro cavities.

4. Digitization of pore structure

4.1. Workflow model

Fig. 6 illustrates the workflow model employed for acquiring the 3D microstructure from the grey image stack. The model comprises a series of steps aimed at obtaining reliable data for comprehensive analysis. Initially, data acquisition is carried out by manufacturing a full-scale frustum shaped ceramic filter, enabling the collection of actual flow rate, mechanical properties (such as strength), and filtrate quality. These data serve to validate the numerical models. Subsequently, subsamples are prepared for scanning using a micro-CT scanner, resulting in the acquisition of an image stack from the scanned sample. Upon obtaining the image stack data, it undergoes processing to prepare it for numerical simulations. To achieve this, a small subset is extracted by cropping the image stack, and the size of the subsample is determined using the REC concept for porosity measurement. Following the sampling process, image conditioning is performed to eliminate noise and artifacts, ensuring reliable simulations, and facilitating visual inspection and validation of the processed data.

Subsequently, the data is manipulated to extract the geometric features of the pore space within the ceramic sample. This involves segmenting the image stack to isolate the pore space and material matrix, as well as binarizing the image stack. The binarized image stack is then utilized to generate the three-dimensional pore structure of the porous ceramic material. In the subsequent step, porosity, tortuosity, and other topological features are extracted from the resulting three-dimensional structure. Additionally, fluid properties such as permeability and flow rate are derived using numerical simulations based on computational fluid dynamics (CFD) solvers. These properties are referred to as simulated properties in this context, contributing to a comprehensive understanding of the ceramic material's behaviour.

4.2. Contrast enhancement

Image segmentation is the process of distinguishing the regions of pore space as one region and material matrix as the region. Once the regions are separated and assigned to a region, it becomes possible to calculate the geometric features of the image as well as the fluid properties inside the pore space. The process of image segmentation is highly dependent on user input based on visual justification [35].

Contrast enhancement improves the visual inspection of scanned image by enhancing the brightness difference in an image and it stretches the grey level from minimum value to maximum value of the image based on the quality of image. Now the image is modified with a tonal enhancement to improve the quality of image for visual inspection. It can be concluded that contrast stretch is used to improve the brightness levels uniformly across the image and tonal enhancements is used to improve the brightness differences in the shadow (dark), midtone (grey), or highlight (bright) regions at the expense of the brightness differences in the other regions. For low contrast images obtained in micro-CT along with artifacts and partial volume effect (PVE) (Bruker, 2017) hinder the segmentation process. Further image processing techniques tend to degrade the contrast with suppression of noise [36]. which necessitates contrast enhancement before applying image processing techniques. Various techniques are available for contrast enhancement based on spatial domain and frequency domain [37]. Contrast improvement which is based on accurately measurements of contrast limited adaptive histogram equalization is applied in this study as shown in Fig. 7 [38]. CLAHE is also an

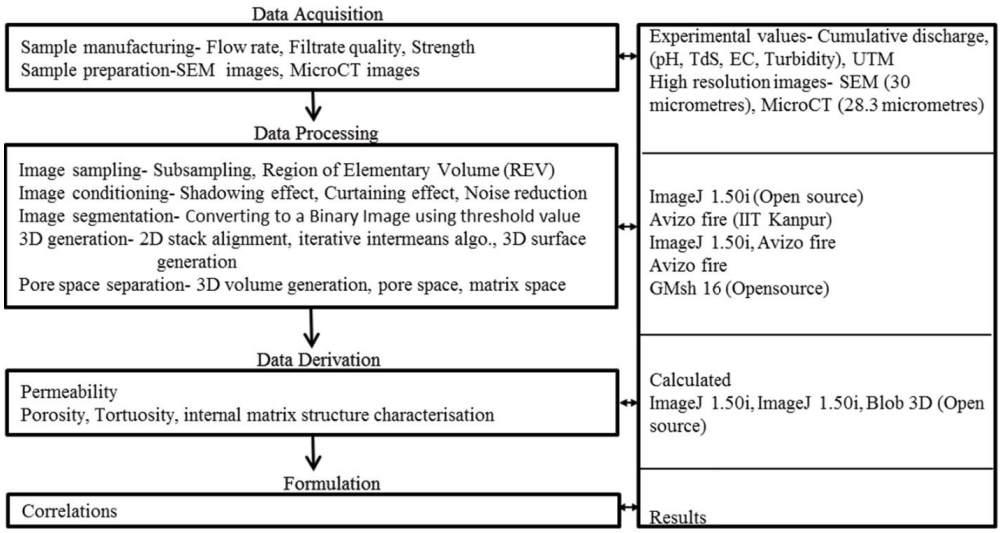

Fig. 6. Digitization of pore structure: flow chart for converting micro-CT images to 3D structure and simulation for permeability.

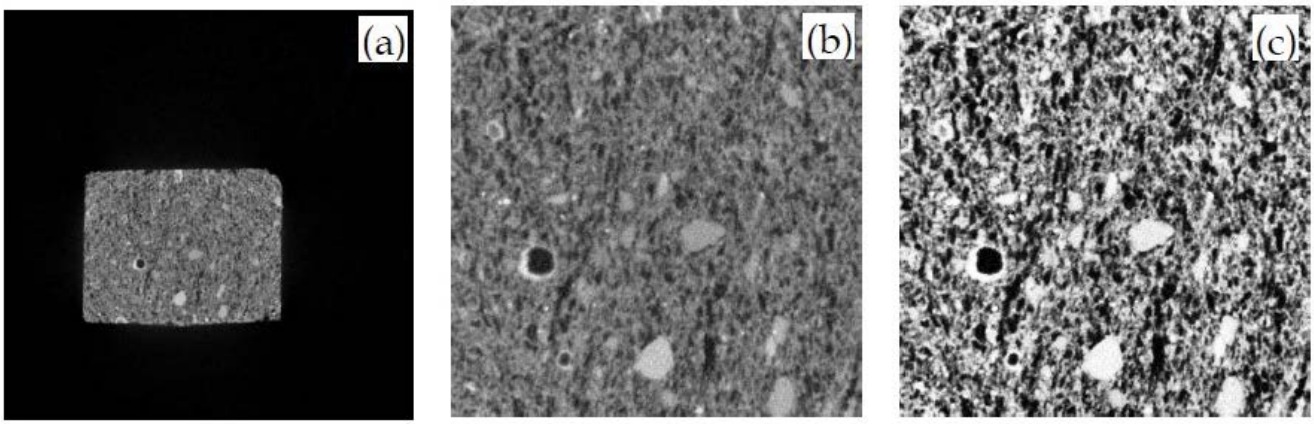

Fig. 7. (a) Scanned image from micro-CT, (b) cropped image and (c) contrast enhancement using CLAHE.

image pre-processing technique which is used to improve contrast in images. CLAHE algorithm computes the histograms of the image at various regions and then redistribute the luminance values of the image. It is used to improve the local contrast of image at smaller regions, and it enhances the edges of the objects in an image. The technique is applied through plugin available in ImageJ software [39].

5. Image processing

5.1. Resolution

Resolution of images acquired using micro-CT images have great impact on the qualitative and quantitative analysis of images and subsequent simulations. Permeability can alter by many folds if resolution of micro-CT scanner is more than the typical size of the grains of material [40]. At the same time, if high resolution is used one must compromise with the REV. Material used in this study contains the microstructure ranging from nano-meter sale to milli-meter scale as evident from SEM images, which represents the heterogeneity in the pore topology. To capture the sufficient volume during the scanning, resolution kept at 28.3 μm per voxel. Error occurred due to low resolution is normalized with extrapolated values obtained from literature for permeability [41].

5.2. Reconstruction of 3D image

Once the 2-dimensional image stack is obtained, next step is to generate 3D pore structure and mesh generation for fluid flow analysis. Various process involved in generation of surface structure are shown in Fig. 8. Avizo software is used generate the surface body. Conversion of 2D image into 3D surface structure is taken care by software and its implementation can be referred in literature [42].

After the surface is generated, simplification and mesh repairing of surfaces are required to reduce the number of individual surfaces and to obtain a watertight body. Watertight body is a type of topology used by computer graphics in which all the surfaces are completely closed and surface normal is always point out from each surface. Simplification of surface can reduce the computation power drastically. Mesh repairing involves various steps and they are applied repeatedly until the watertight body is obtained. Various steps are applied to repair the geometry and checked for watertight body. Once the geometry is checked for watertight body, it becomes clean for the numerical simulation. To get the clean geometry and watertight body, these iterative steps are suggested.

In the context of surface mesh generation, a surface mesh is composed of interconnected triangles, where each triangle is linked to adjacent triangles through nodes. It is common for a surface mesh to encompass multiple continuous surfaces, which ideally should be seamlessly joined together. However, during the mesh generation process, certain nodes become obsolete and need to be eliminated. To achieve a high-quality surface mesh, several steps are undertaken, as follows. Firstly, the mesh is examined for any holes or gaps, which are subsequently closed and bridged to ensure topological coherence. Singular edges and vertices, which may disrupt the mesh connectivity, are then identified and fixed. Overlaps and intersections between points and surfaces are resolved to eliminate any geometric inconsistencies.

Furthermore, the mesh is subjected to a filtering process to remove unwanted elements such as double faces, double vertices, inverted normal (indicating surfaces facing inward), and skewed or small triangles. Open edges and holes in the mesh are stitched together to create a continuous surface. Manual repair techniques are employed, involving visual inspection of the mesh, followed by the deletion and creation of triangles at boundaries where necessary. Finally, re-meshing operations are performed to optimize the overall triangle count, ensuring an efficient representation of the surface geometry. These procedures collectively contribute to the production of a high-quality surface mesh, which accurately represents the underlying surfaces and meets the desired criteria for research and analysis.

5.3. Grid generation

Once the surface mesh is generated for the porous structure, volume mesh file is generated in the region of void spaces. Volume mesh is used in numerical simulation. To achieve volume mesh, at first surface mesh is created in void space and then volume mesh is generated inside

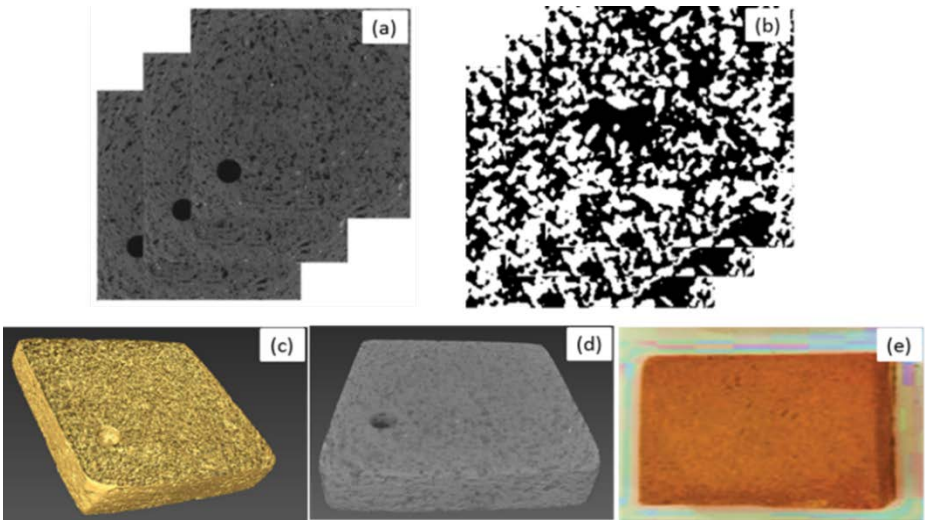

Fig. 8. Reconstruction of 3D microstructure (a) 2D image stack, (b) binary image stack, (c) 3D surface body, (d) 3D volume body and (e) original sample image.

this closed surface mesh. This step is performed on open-source software named Gmesh. Workflow to generate three-dimensional mesh from watertight body is shown in Fig. 9.

Generation of surface mesh to volume mesh is shown in Fig. 10. Approx. 20 million nodes are generated in fluid region (where pore space was present prior to volume generation.) after the simplification and repairing of material surface. Simplification step only reduces the number of compute node from approximately 74 million to 20 million, thus reducing the computational power drastically. After the simplification process, surface suffers from defects as opening of closed surface at various locations. These meshes are required to be repaired again. Digital structure is used to identify the pore space and mesh is generated for flow simulation in Fig. 8.

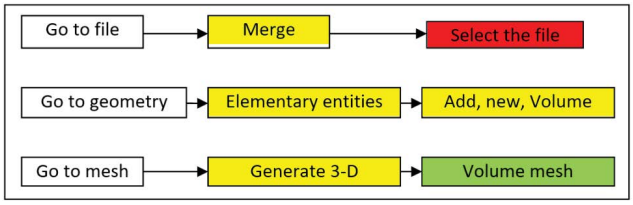

Fig. 9. Workflow to generate volume mesh from watertight body.

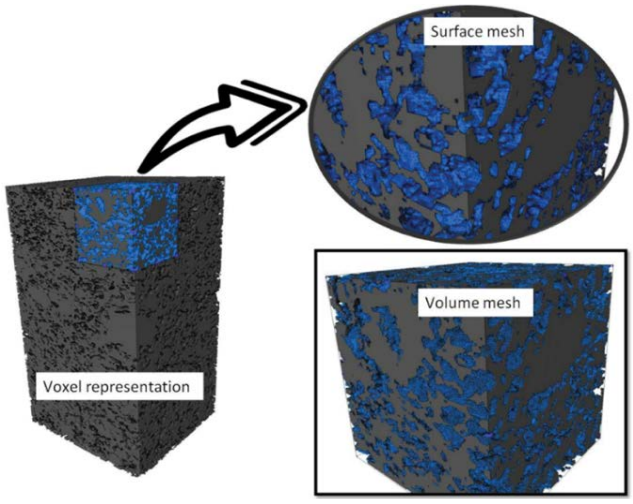

Fig. 10. Voxel representation of data, generated surface mesh and converted volume mesh (represented in blue colour).

6. Simulation

6.1. Numerical solution of ns equation

Computational domain (geometry) is discretised. At first the surface of the geometry is discretised and then volume discretisation takes place to generate the node points in the entire domain. These nodes are used for the computation. Cell is formed using these nodes and it is called the grids or mesh. These grid cells can be polyhedrons, usually tetrahedrons, hexahedrons, prisms, or pyramids (Here tetrahedrons are used for discretisation). As a result of numerical solution of model equations for fluid flow, the sought flow parameters are obtained just at the grid nodes [43]. In present study, tetrahedral grids are used to discretize the fluid domain as shown in Fig. 11a. Once the mesh is generated boundary conditions are applied to the domain to initiate the solution iterative process. In simulations, following boundary conditions are applied as shown in Fig. 11b. In the numerical simulation model used to study the microchannel flow, the boundary conditions are specified as follows. At the inlet, a relative pressure inlet condition is applied, with a range of 0.02646 to 0.000294 bar. This represents the pressure difference between the inlet and the surrounding environment. The outlet boundary is set as a relative pressure outlet condition, with a value of 0 bar, indicating that the pressure at the outlet is equal to the ambient pressure. The side walls of the microchannel are treated as symmetry boundaries, implying that the flow properties parallel to these walls remain constant and

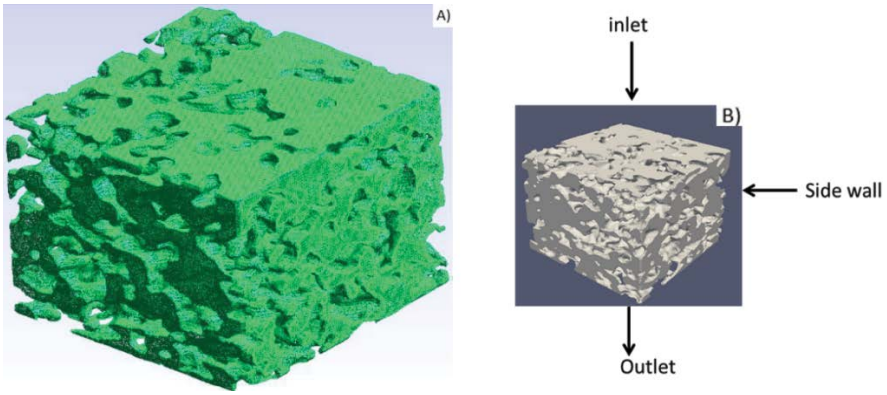

Fig. 11. Computational domain (a) surface mesh and (b) boundary condition.

do not exhibit any variations. These boundary conditions play a critical role in accurately capturing the behaviour and characteristics of the fluid flow within the microchannel, enabling insightful analysis and interpretation of the results.

6.2. Solver-stokes equation

$$\begin{cases} \vec{\nabla}\cdot\vec{V}=0 \\ \mu\nabla^2\vec{V}-\vec{\nabla}P=\vec{0} \end{cases} \tag{4}$$

In the context of microchannel flow, the Navier–Stokes equations system is modified by applying several assumptions to simplify the governing equations. Firstly, the fluid is assumed to be incompressible, resulting in a constant density throughout the flow field. Additionally, the fluid is assumed to exhibit Newtonian behavior, where the dynamic viscosity is considered to be a constant value. The flow is assumed to be in a steady state, implying that there is no temporal change in velocity over time. Furthermore, the flow is assumed to be in the laminar regime, as the Reynolds number within the pores is significantly lower, indicating a dominance of viscous forces over inertial forces. These assumptions enable the simplification of the Navier–Stokes equations and provide a framework for analyzing microchannel flow with enhanced computational efficiency and accuracy [44].

The equation systems cannot be solved using fully implicit methods (matrix inversion) because the matrices of this kind of system are singular. Therefore, an artificial compressibility coefficient and sometime derivative terms are introduced in the system to converge the solution [45]. By adding the artificial compressibility factor into the pressure gradient terms converts the nature of momentum conservation equation from elliptical incompressible to the compressible hyperbolic. Now the momentum equation can be solved by standard, implicit, time marching methods which ensures the convergence of solution. Artificial compressibility can be regarded as the speed of sound in the fluid medium. Finite volume method is applied to solve the equation systems. The equations are discretized on a staggered grid, allowing a better estimation of the no-slip boundary condition. Pressure unknowns are located at the centre of the voxel while velocity unknowns are decomposed at the faces of the voxels. Once the simplified system of equation is solved, permeability coefficient is evaluated by applying Darcy's law and correction factor for the simulated permeability is estimated form experimental permeability value. This correction coefficient is used to correct the velocity profile in microstructure due to limitation of finite resolution of micro-CT images. These results will be used to predict the filter efficiency. Permeability is calculated on the 3D geometry obtained from the image stack using the Eq. (5) [46].

$$\kappa=\frac{1}{R}\left(\frac{N_x}{N_yN_z}\right)\frac{Q\mu}{\Delta P} \tag{5}$$

where, K is permeability, R is resolution of image stack, N_x is number of voxels in the direction of flow, N_y and N_z are number of voxels in other two direction, Q is flow rate and P is pressure.

7. Results and discussion

7.1. Results from digital pore structure (tomography based micro-structural analysis)

Digital internal micro-structure analysis involves the quantifying pore space information based on single image or image stack obtained by various methods [47]. Single image helps measurement of porosity (in two-dimensional space) whereas image stack helps the construction of three-dimensional structure of pore space [47]. However due to limitation of two-dimensional analysis, micro computed tomography (micro-CT) based three-dimensional pore structure imagery has been studied in this work [48]. 3D digital structures can also be used for numerical simulation of flow field and determination of flow properties based on various simulation techniques [48,49].

In Table 1 microstructural quantities of images (28.3 μm resolution micro-CT, Procon X-Ray CT-mini) of 55R and 50R before and after filtration events were obtained. The retrieved images were processed using ImageJ TM software (Schneider CA 2012) for segmenting the grey images into binary images using iterative inter-means method [50]. At this stage, images are combined to construct 3D structure

and subsequent topological analysis performed using 3D viewer module available in ImageJ [51]. Various quantization parameters can be derived from such digital three-dimensional porous structure [52].

7.2. Simulation results

Flow field inside the porous media can be simulated assuming Stokes flow inside of micro cavities. Avizo 6.0 software is used to predict the permeability of filter material after each run and compared with the experimental values. Simulation results with velocity flow field and permeability are shown in Fig. 12 (above and below) for 50R and 55R, respectively. Values of simulated permeability is tabulated in Table 2. To find the correlation between simulated values and experimental values. It shows the trends from the simulation results follow the same pattern.

Table 2
Values of simulated and experimental permeabilities

S. No.	Sample	Simulated permeability (in m^2)	Experimental permeability (in m^2)	Correction factor (CF)
1	45S3R1	361.37	0.0617	0.00017
2	45S1R2	427.57	0.08311	0.00019
3	45S2R3	431.46	0.03634	0.00008
4	45S2R7	259.34	0.03453	0.00013
5	50S2R1	310.74	0.05392	0.00017
6	50S3R2	479.75	0.09108	0.00019
7	50S1R3	216.51	0.05429	0.00025
8	50S1R7	209.5	0.05102	0.00024
Av. correction factor				0.00018

Table 1
Microstructural quantification and change in three-dimensional microstructure of ceramic ware with cyclic loading

Sample name	Porosity (%)	Total surface area (mm^2)	SNSVR	Aspect ratio	Major axis length (mm)	Minor axis length (mm)	Tortuosity
55S0R0*	54.24687	1,881.523	1.5643	1.647551	0.106566	0.048695	4.261792
55S1R2	53.38923	1,865.566	1.544935	1.626186	0.115933	0.053952	3.578243
55S3R1	54.20803	1,810.616	1.559108	1.547779	0.113248	0.053247	3.791654
55S2R3	53.17275	1,797.563	1.55557	1.479413	0.103885	0.048642	4.515614
50S1R3	56.23543	1,958.307	1.542945	1.642193	0.107253	0.050722	4.477668
50S2R1	53.46891	1,872.036	1.553004	1.618223	0.105639	0.047813	4.450685
50S0R0*	61.62486	1,858.064	1.583462	1.768933	0.114307	0.049295	13.39457
50S3R2	54.16708	2,040.071	1.553628	1.592842	0.097248	0.044217	5.341406

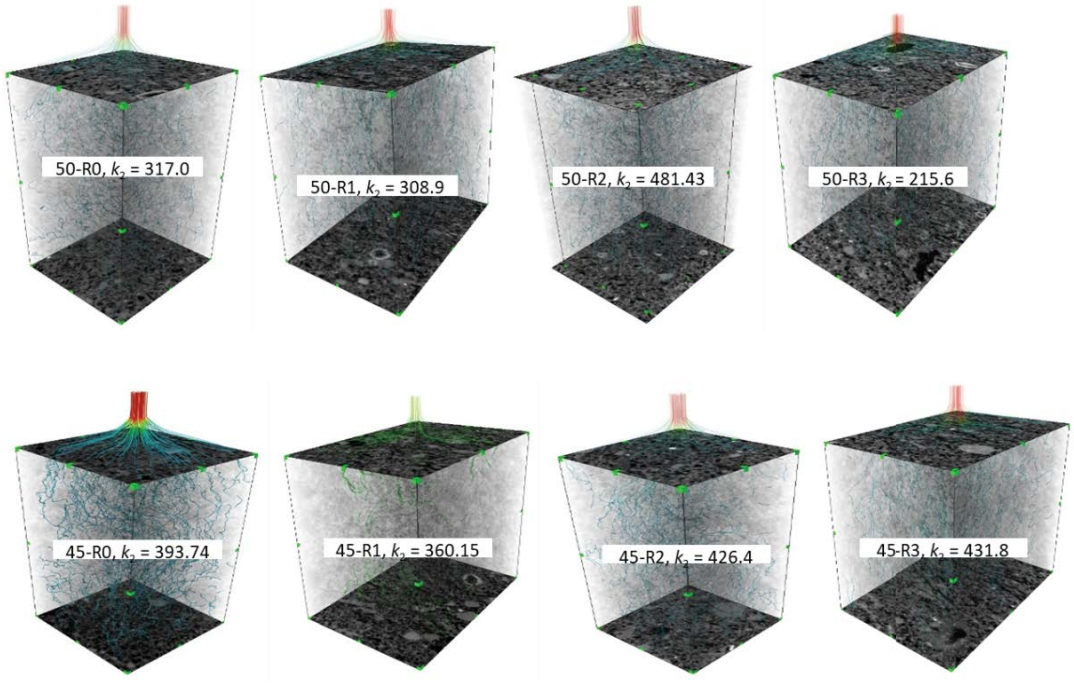

Fig. 12. Permeability of 50R sample (above), permeability of 55R sample (below).

The difference between the experimental results and experimental results occurs during the scanning stage of the sample using micro-CT scanning. These errors are attributed due to the resolution limit of the micro-CT scanner which is taken as 28.7 μm in our study to capture the sufficient large RoI of the sample. Since the patters are same in both results, correction factor can be defined to eliminate the errors in the simulated results and modified simulated values can be used to determine the other derived properties which are not possible or difficult to achieve with experimental procedure like adsorption phenomenon with long term filtration process.

7.3. Correlation between experimental permeability and simulated permeability

Experimental values and simulation results shows the same trend for a given material; however higher values of permeability are obtained in comparison to the experimental values as shown in Fig. 13. Comparison in permeability values is performed for both compositions of 50C:50S and 55C:45S denoted as 50SnRn and 45SnRn, respectively where n denotes the number of runs. From Fig. 13 it can be observed that after 3rd run flow rate shows becomes steady and gradual decrease in flow rate is observed due to decrease in porosity. Ratio of experimental and simulated permeability can be used to predict the life period of ceramic filter as discussed during the sustainability of filter in subsequent points. Average Correction factor (CF) = 0.00018:

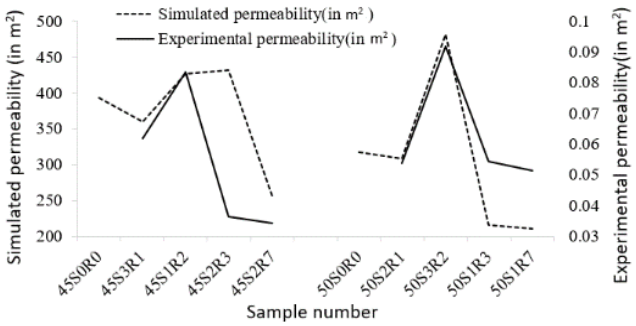

Fig. 13. Experimental (right) and simulated (left) values of permeability.

$$\text{Correction Factor}(\text{CF}) = \frac{\text{Experimental permeability}(k_e)}{\text{Simulated permeability}(k_s)} \quad (6)$$

Correction factor is calculated by normalizing the simulated values with the experimental values as a reference. Correction factors are tabulated in Table 2. These values can be used to offer the correction factor. While calculating the efficiency of these filters.

7.4. Long term treatment efficiency

Permeability depends on the porosity of ceramic filter. With the use of ceramic filter, physical contaminants in the form of suspended particulate and organic contaminants will generate the resistance for the flow rate of filtrate through filter further [15]. Such change in permeability will extensively depend on turbidity of the infiltrate and efficiency to remove such suspended particle through filter. Trapping of particulate will result in decrease in porosity and subsequent decrease in permeability due to formation of flocs [53]. Long term usage of filter will require to treat filter by re-burning it at elevated temperature so that suspended particulate can resettle on the surface of micro cavity and water can percolate again [14].

Effect of permeability for long term usage of filter can be evaluated by simulations. We performed simulations to predict the permeability on same microstructure while changing its porosity numerically and decreasing gradually as shown in Fig. 14. The figure shows the velocity field (depicted by path lines) inside the porous structure. Decrease in flow rate can be observed with decrease in porosity of microstructure.

7.5. Correlation between permeability with porosity

These permeability values were mapped with the reference permeability (obtained experimentally after third run when flow patterns become steady) to overcome the limitation of finite resolution of scanned data using Eq. (7) of permeability.

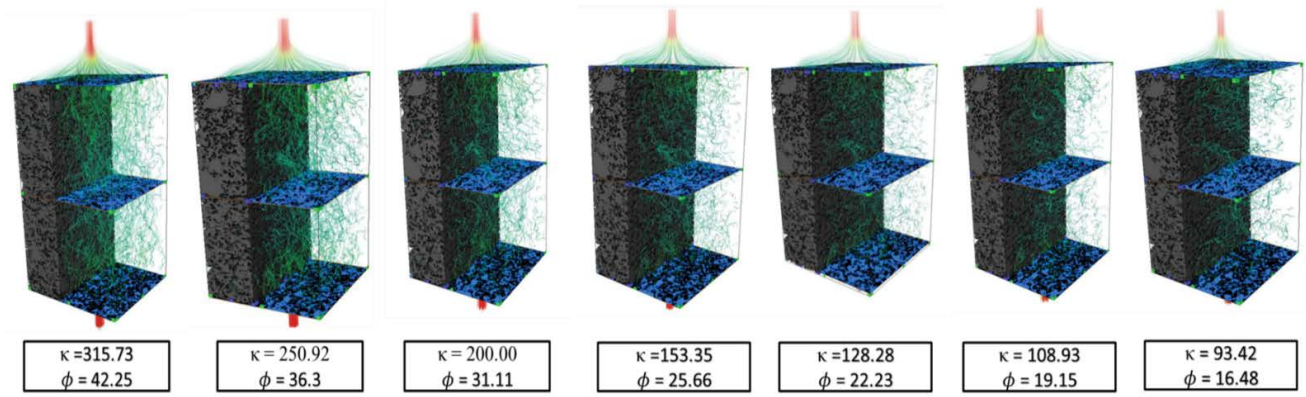

Fig. 14. Permeability values form from left to right figures for decreasing porosity values.

$$\text{Permeability}(\kappa) = -0.035\ln(\phi) + 0.0882 \quad (7)$$

It is evident from Fig. 15. that there is rapid decrease in permeability initially due to decrease in porosity of the material. With the use of filter permeability decreases and after some time it shows the asymptotic behaviour for flow rate. At such time re-burning of filter is required to maintain its flow rate of filtrate again.

7.6. Lifetime of ceramic filter

The longevity of a ceramic filter is contingent upon the properties of the ceramic material and the quality of the inlet water, as indicated in Table 5. To determine the filter's lifespan, the CEC and the concentration of contaminants in the inlet water are computed. These factors play a crucial role in assessing the filter's ability to effectively remove impurities and maintain its filtration efficiency over time. By analysing the CEC and the contamination concentration of the inlet water, one can estimate the filter's durability and make informed decisions regarding its replacement or maintenance. These calculations provide valuable insights into the expected lifespan of ceramic filters and aid in optimizing their performance for water purification applications.

7.6.1. Cation exchange capacity

CEC is a measure of charge present at the surface of the clay. CEC values are calculated for samples at various temperatures as discussed in Table 2. It shows that beyond the 450°C temperature and up to 850°C, CEC value starts decreasing quickly due to formation of metakaolinite and spinel at later stage as shown in Fig. 16. At 850°C, stable mullite starts forming CEC remains almost constant [54]. At 850°C, stable mullite starts forming and CEC remains almost constant. CEC values are calculated for samples at various temperature.

CEC is defined as the capacity of the sample (here ceramic membrane) to adsorb the ions which are usually cations (because the clay holds the negative charge at its surface under atmospheric condition. However, at very low pH value, it may contain positive charge at the surface). Sample becomes able to exchange counter species in a reversible chemical reaction by neutralizing the negative charge in the soil. The higher the CEC, the more cations it can retain. It can be expressed in terms of milli-equivalents/100 g of soil (or 100 meq/g) [55]. CEC is determined using the reference solution conditions (buffered to pH 7) accepted universally in order to reduce the errors generated under various experimental condition. Various methods are available to determine CEC. Proper method of determining the CEC is based on the type of colloidal material involved in the cation exchange of the soil [56].

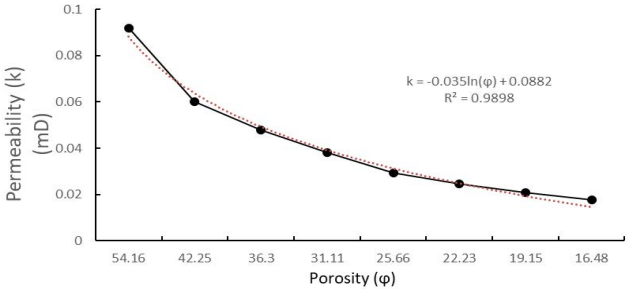

Fig. 15. Correlation between permeability with porosity.

The determination of CEC involves a series of steps as follows. Initially, a 5 g sample is taken and mixed with 1 molar NH_4OAc (ammonium acetate) solution, allowing it to soak overnight in a centrifuge tube. The sample is then rinsed with isopropanol and 1 M KCl solution. Subsequently, the sample is transferred to a beaker and washed with 30 mL of 1 M NH_4OAc solution using a filter paper (size 42). This rinsing process is repeated three times, followed by another rinse with 40 mL of isopropanol and 1 M NH_4OAc solution. The third rinse step is also repeated three times. Finally, the sample is rinsed with 50 mL of 1 M KCl solution, and the solution is made up to a total volume of 250 mL. The concentration of ions in the solution is determined using colorimetry by comparing it with a known solution of KCl. These steps ensure the accurate measurement of CEC in the samples, providing valuable insights into their ion exchange capacities and their potential for water purification applications.

Results are tabulated in Table 3 for different samples prepared at different temperature. For the calculation purpose, value of CEC is taken as 11.0 meq/100 g (at 800°C).

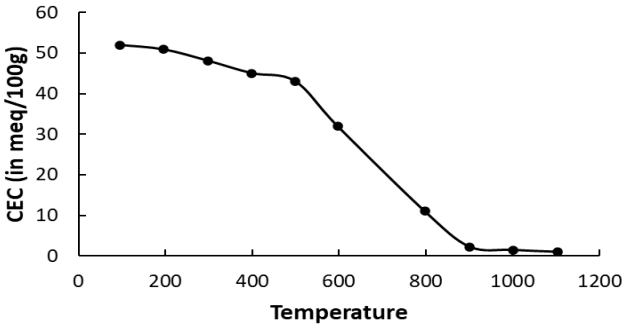

Fig. 16. Cation exchange capacity of clay with varying temperature.

Table 3
CEC values at different temperature

Temperature	CEC (in meq/100 g)
94	51.95
196	50.88
297	48.11
398	45.02
498	43.06
596	32.02
797	11.01
901	2.26
1,000	1.45
1,103	0.98

7.7. Brunauer–Emmett–Teller

Specific surface areas for samples are evaluated using Brunauer–Emmett–Teller (BET) analysis [57]. Changes in specific areas are recorded for change in sintering temperature of the samples using the adsorption/desorption curves. BET curve for 50:50 sintered ceramic is shown in Fig. 17. Specific surface areas for samples are evaluated using BET analysis. Whereas specific surface area, and CEC of the samples are tabulated in Table 4 against the temperature of the samples.

7.8. Surface charge density

Maximum permissible temperature for baking ceramic filters. If the temperature is elevated more than 850°C, ceramic filter with 50C composition will lose its functionality [58]. In the same manner, if the temperature is quite low (650°C–700°C), isomorphous substitution of K^+, Na^+, Mg^{++}, Ca^{++} and other fluxing agent will not take place and filtered water will contain these ions and water will become more brackish in nature. Again, optimum temperature range between 700°C–850°C depends on the fluxing element which reduce the forming temperature of spinel and mullite. If lower amounts of fluxing agents are present in the clay, one should use the higher bound of temperature range (700°C–850°C) and if higher amounts of fluxing agents are present in the clay, one should use the lower bound of temperature range.

In this study, temperature is kept at around 800°C for comparatively large time duration to ensure the proper substitution and avoiding the formation of mullite. It should be noted that temperature inside the ceramic material is bit lower than the surface temperature which is at 800°C. Under such condition, CEC value is calculated to be 11.0 meq/100 g of sintered samples. This value of CEC can be converted to the surface charge density in C/m^2 if specific surface area is known [59]. In present study, value of CEC and surface charge density is taken as and respectively. In present study, value of CEC and surface charge density is taken as 11.01 meq/100 g and 0.3232 C/m^2.

7.9. Quality of inlet water

Quality of drinking water is set by Bureau of Indian Standards [60]. Various parameters are set to ensure the safe drinking water including pH, TDS, salt concentration and turbidity. To test the filtration efficiency of these ceramic filters, a solution of known contaminant is prepared and filtered through these filters. Solution is prepared by adding $CaCl_2$, $Ca(OH)_2$, $CaSO_4$, $MgCl_2$, $Mg(OH)_2$ and $MgSO_4$ salts at 20.7°C. Parameters are checked for inlet water and outlet water as shown in Table 3. From experiments conducted in filter, number of species present in water are 6 and the absorbing capacity of filter can be determined from Table 5. The filtration efficiency of the G-filter with additive materials for specific ions is also documented. The results indicate that the readings are significantly below the maximum limits prescribed for drinking water, ensuring the effectiveness of the filtration process. The water samples analyzed in this study contained a total of six different species, including equal molar concentrations of $CaCl_2$, $Ca(OH)_2$, $CaSO_4$, $MgCl_2$, $Mg(OH)_2$ and $MgSO_4$. The volume of water used in each filter was standardized at 12 L, ensuring consistency in the experimental setup. These findings provide valuable insights into the filtration performance of the G-filter and its ability to meet the required standards for safe drinking water.

7.10. Calculating life of ceramic filter

7.10.1. Evaluation of life of a ceramic filter

The lifetime of a filter can be accurately predicted by considering two critical parameters: firstly, the filter's efficiency in effectively treating water to the desired level of contaminant removal, and secondly, its ability to maintain an adequate water flow rate throughout its operational lifespan. These parameters are essential in ensuring the long-term effectiveness and reliability of the filtration system. By assessing the filter's contaminant removal efficiency and its ability to sustain a consistent water flow rate, researchers and practitioners can make informed decisions regarding the appropriate lifespan and maintenance of the filter. This predictive approach enhances the overall performance and

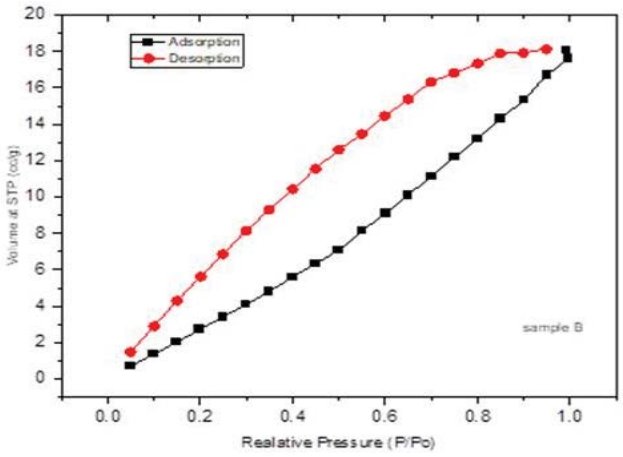

Fig. 17. Brunauer–Emmett–Teller curve for 50:50 sample.

Table 4
Surface charge density at different temperatures volume at STP (cc/g)

Temperature (In °C)	Surface area (In m^2/100 g)	CEC (In meq/100 g)	Surface charge density (In C/m^2)
94.91	4,309.24	51.95	1.1612
196.18	5,896.06	50.88	0.8311
297.57	5,158.65	48.11	0.8984
398.98	6,179.03	45.02	0.7017
498.94	8,907.77	43.06	0.4657
596.79	4,786.41	32.02	0.6444
797.88	3,281.59	11.01[a]	0.3232
901.04	1,850.58	2.26	0.1174
1,000.93	1,310.72	1.45	0.1064
1,103.53	407.59	0.98	0.2307

[a]This value is used for further calculations as a reference value.

Table 5
Quality of filtrate from ceramic water filter

S. No./Parameter		Measured water parameter				
		pH	Total dissolved solids (ppm)	Salt (ppm)	Conductivity (Micro Siemens)	Turbidity (NTU)
Requirement (acceptable limit) as per IS 10500:2012		6.5 to 8.5	500	200	1,050	
1	Inlet sample	9.81	934	750	1,340	801
2	Outlet sample	8.81	492	384	701	76.6
	Reduction (%)	10.19	47.32	48.80	47.68	90.40

sustainability of water treatment systems, contributing to improved water quality and public health outcomes.

Efficiency will depend on CEC value of sintered filter and its absorption on cations on its surface. Lifetime based on treatment efficiency has been formulated for contaminated water having known chemical impurity (equal molar concentration of $CaCl_2$, $Ca(OH)_2$, $CaSO_4$, $MgCl_2$, $Mg(OH)_2$ and $MgSO_4$ and its treatment efficiency of salt removal for single run-on field scale ceramic filter. If we assume all cations present in contaminated water is divalent then total moles of cations (++) absorbed by filter from one litre of contaminated water can be evaluated as follows [61].

$$M = \frac{2n}{\sum z}\left(\frac{p}{10^3}\right) \tag{8}$$

Amount of water treated by ceramic material:

$$m = \frac{q}{2} \times M \times \left(10w\right) \tag{9}$$

If we assume water can be filled two times a day, then lifetime of filter:

$$d = \frac{m}{2V \times 365} \tag{10}$$

Correlation between porosity and permeability of porous structure having microstructure can be represented as in Eq. (7).

8. Conclusion

The correlation between porosity and permeability in porous structures with microstructure can be represented by the proposed relation. The lifetime of a ceramic filter is influenced by the activity of the ceramic material and the quality of the inlet water. It can be calculated by considering the CEC and the concentration of contaminants in the inlet water. The CEC values are determined at various temperatures, with stable mullite formation observed at 850°C leading to nearly constant CEC values. Additionally, the specific surface areas of the samples are evaluated using BET analysis. The water used in the experiments contains six different species, with equal molar concentrations of $CaCl_2$, $Ca(OH)_2$, $CaSO_4$, $MgCl_2$, $Mg(OH)_2$ and $MgSO_4$. A volume of 12 L is considered for one filter. The comparison between experimental and simulation results is conducted, and a correction factor (CF) is introduced to eliminate errors caused by the low resolution of micro-CT imaging. The CF is calculated by normalizing the simulated values with the experimental values as a reference. The flow rate through the porous media can be determined by considering the wet area (A), pressure gradient (∇p), fluid viscosity (μ), and porous media thickness (Δx). The permeability value (K) can be calculated using Kozeny's–Carman equation. Furthermore, the lifetime of gravity filters is dependent on the density of active sites within the ceramic material, which can be evaluated through CEC experiments. The analysis of sintered porous structures involves assessing their microstructure to understand their flow characteristics. Experimental permeability measurements are compared with simulated values obtained through micro-CT imaging, allowing for a comprehensive understanding of the flow behaviour in the porous media. Additionally, electro-kinetic treatment is applied to estimate the adsorption of ions on the negatively charged porous sintered ceramic, providing insights into the behaviour of contaminants in the porous structure.

References

[1] A.L. Bulta, G.A.W. Micheal, Evaluation of the efficiency of ceramic filters for water treatment in Kambata Tabaro zone, southern Ethiopia, Environ. Syst. Res., 8 (2019) 1, doi: 10.1186/s40068-018-0129-6.
[2] C. Farrow, E. McBean, G. Huang, A.L. Yang, Y.C. Wu, Z. Liu, Z.N. Dai, H.Y. Fu, T. Cawte, Y.P. Li, Ceramic water filters: a point-of-use water treatment technology to remove bacteria from drinking water in Longhai City, Fujian Province, China, J. Environ. Inf., 32 (2018) 63–68.
[3] P.-M. Nigay, A.A. Salifu, J.D. Obayemi, C.E. White, A. Nzihou, W.O. Soboyejo, Ceramic water filters for the removal of bacterial, chemical, and viral contaminants, J. Environ. Eng., 145 (2019), doi: 10.1061/(ASCE)EE.1943-7870.0001579.
[4] S. Mauran, L. Rigaud, O. Coudevylle, Application of the Carman–Kozeny correlation to a high-porosity and anisotropic consolidated medium: the compressed expanded natural graphite, Transp. Porous Media, 43 (2001) 355–376.
[5] N.L.Q. Cuong, N.H. Minh, H.M. Cuong, P.N. Quoc, N.H. Van Anh, N. Van Hieu, Porosity estimation from high resolution CT SCAN images of rock samples by using housfield unit, Open J. Geol., 8 (2018) 1019–1026.
[6] D. Mašín, C. Tamagnini, G. Viggiani, D. Costanzo, Directional response of a reconstituted fine-grained soil—Part II: performance of different constitutive models, Int. J. Numer. Anal. Methods Geomech., 30 (2006) 1303–1336.
[7] A. du Plessis, C. Broeckhoven, A. Guelpa, S.G. le Roux, Laboratory X-ray micro-computed tomography: a user guideline for biological samples, Gigascience, 6 (2017) 1–11.

[8] C. Tien, B.V. Ramarao, Can filter cake porosity be estimated based on the Kozeny–Carman equation?, Powder Technol., 237 (2013) 233–240.
[9] A. Reichenbach, et al., Finding and discussion, Prog. Retin. Eye Res., 561 (2019) S2–S3.
[10] H. Yang, S. Xu, D.E. Chitwood, Y. Wang, Ceramic water filter for point-of-use water treatment in developing countries: principles, challenges and opportunities, Front. Environ. Sci. Eng., 14 (2020) 79, doi: 10.1007/s11783-020-1254-9.
[11] A.T. Ajibade, M.B. Amuda, O.T. Olurin, Dividend policy and financial performance – a study of quoted manufacturing firms in Nigeria and Kenya, South Asian J. Social Stud. Econ., 3 (2019) 1–8.
[12] D.W. Robert, Development of a Ceramic Water Filter for Nepal, Massachusetts Institute of Technology, Master Thesis, 2013, p. 170.
[13] B.A. Ajayi, Y.D. Lamidi, Formulation of ceramic water filter composition for the treatment of heavy metals and correction of physiochemical parameters in household water, Art Des. Rev., 3 (2015) 94–100.
[14] S. Gupta, R.K. Satankar, A. Kaurwar, U. Aravind, M. Sharif, A. Plappally, Household production of ceramic water filters in Western Rajasthan, India, Int. J. Serv. Learn. Eng. Humanit. Eng. Soc. Entrep., 13 (2018) 53–66.
[15] I. Yakub, A. Plappally, M. Leftwich, K. Malatesta, K.C. Friedman, S. Obwoya, F. Nyongesa, A.H. Maiga, A.B.O. Soboyejo, S. Logothetis, W. Soboyejo, Porosity, flow, and filtration characteristics of frustum-shaped ceramic water filters, J. Environ. Eng., 139 (2013) 986–994.
[16] Q. Xiong, T.G. Baychev, A.P. Jivkov, Review of pore network modelling of porous media: experimental characterisations, network constructions and applications to reactive transport, J. Contam. Hydrol., 192 (2016) 101–117.
[17] E. Walker, P.W.J. Glover, Permeability models of porous media: characteristic length scales, scaling constants and time-dependent electrokinetic coupling, Geophysics, 75 (2010) E235–E246.
[18] A.A. Mohamad, Chapter 11 – Combustion in Porous Media: Fundamentals and Applications, D.B. Ingham, I. Pop, Eds., Transport Phenomena in Porous Media III, Elsevier Ltd., Oxford, United Kingdom: Pergamon, 2005, pp. 287–304, doi: 10.1016/B978-008044490-1/50015-6.
[19] A. Jahanbakhsh, K.L. Wlodarczyk, D.P. Hand, R.R.J. Maier, M.M. Maroto-Valer, Review of microfluidic devices and imaging techniques for fluid flow study in porous geomaterials, Sensors (Switzerland), 20 (2020) 4030, doi: 10.3390/s20144030.
[20] S. Khirevich, M. Yutkin, T.W. Patzek, Correct estimation of permeability using experiment and simulation, Phys. Fluids, 34 (2022) 123603, doi: 10.1063/5.0123673.
[21] S. Gärttner, F.O. Alpak, A. Meier, N. Ray, F. Frank, Estimating permeability of 3D micro-CT images by physics-informed CNNs based on DNS, Comput. Geosci., 27 (2023) 245–262.
[22] S.D. Goals, World Health Statistics, 2022.
[23] P.-M. Nigay, A. Salifu, J. Obayemi, C. White, A. Nzihou, W. Soboyejo, Ceramic water filters for the removal of bacterial, chemical, and viral contaminants, J. Environ. Eng., 145 (2019) 04019066, doi: 10.1061/(ASCE)EE.1943-7870.0001579.
[24] A.K. Plappally, J.H. Lienhard V, Costs for water supply, treatment, end-use and reclamation, Desal. Water Treat., 51 (2013) 200–232.
[25] S. Duhan, S.K. Adari, N. Kanwar, S. Gupta, A.K.P.M. Ahmad, P.K. Dammala, M. Chhabra, A.K. Plappally, Suitability of Clayey Soils from Jalore and Jodhpur, Rajasthan, India, for the Production of 3-Litre Ceramic Water Filters, Desalination for the Environment, Clean Water and Energy, Limassol, Cyprus, May 22–May 26, 2023.
[26] M. Ahmad, S. Duhan, R.K. Satankar, A.K. Plappally, Long-Term RELIABILITY assessment of Ceramic Water Filters: Strength and Electro-kinetic Parameter Studies, Proceedings of Desalination for the Environment, Clean Water and Energy, Limassol, Cyprus May 22–May 26, 2023.
[27] D. van Halem, S.G.J. Heijman, A.I.A. Soppe, J.C. van Dijk, G.L. Amy, Ceramic silver-impregnated pot filters for household drinking water treatment in developing countries: material characterization and performance study, Water Sci. Technol. Water Supply, 7 (2007) 9–17.
[28] S. Murcott, Arsenic Contamination in the World: An International Sourcebook 2012, Water Intelligence Online, 2012.
[29] A.K. Plappally, J.H. Lienhard V, Energy requirements for water production, treatment, end use, reclamation, and disposal, Renewable Sustainable Energy Rev., 16 (2012) 4818–4848.
[30] A. Plappally, I. Yakub, L.C. Brown, W.O. Soboyejo, A.B.O. Soboyejo, Theoretical and experimental investigation of water flow through porous ceramic clay composite water filter, FDMP, 5 (2009) 373–398.
[31] E.A. Moreira, M.D.M. Innocentini, J.R. Coury, Permeability of ceramic foams to compressible and incompressible flow, J. Eur. Ceram. Soc., 24 (2004) 3209–3218.
[32] S. Duhan, A.K. Agrawal, A.K. Plappally, Structural and Characterization Assessment of Clay Ceramic Water Filter Materials From Locations Near the Thar Desert in India, Proceedings of Desalination for the Environment, Clean Water and Energy, Limassol, Cyprus May 22–May 26, 2023.
[33] R.G. Loucks, R.M. Reed, S.C. Ruppel, U. Hammes, Spectrum of pore types and networks in mudrocks and a descriptive classification for matrix-related mudrock pores, AAPG Bull., 6 (2012) 1071–1098.
[34] J.M. Carcione, D. Gei, T. Yu, J. Ba, Effect of clay and mineralogy on permeability, Pure Appl. Geophys., 176 (2019) 2581–2594.
[35] P. Iassonov, T. Gebrenegus, M. Tuller, Segmentation of X-ray computed tomography images of porous materials: a crucial step for characterization and quantitative analysis of pore structures, Water Resour. Res., 45 (2009), doi: 10.1029/2009WR008087.
[36] F. Attivissimo, G. Cavone, A.M.L. Lanzolla, M. Spadavecchia, A technique to improve the image quality in computer tomography, IEEE Trans. Instrum. Meas., 59 (2010) 1251–1257.
[37] C.R. Nithyananda, A.C. Ramachandra, Preethi, Review on Histogram Equalization based Image Enhancement Techniques, 2016 International Conference on Electrical, Electronics, and Optimization Techniques (ICEEOT), IEEE, Chennai, India, 2016, pp. 2512–2517.
[38] Z. Al-Ameen, G. Sulong, A. Rehman, A. Al-Dhelaan, T. Saba, M. Al-Rodhaan, An innovative technique for contrast enhancement of computed tomography images using normalized gamma-corrected contrast-limited adaptive histogram equalization, EURASIP J. Adv. Signal Process., 2015 (2015) 32, doi: 10.1186/s13634-015-0214-1.
[39] K. Zuiderveld, Graphics Gems IV, P.S. Heckbert, Ed., Academic Press Professional, Inc., San Diego, CA, USA, 1994, pp. 474–485. Available at: http://dl.acm.org/citation.cfm?id=180895.180940
[40] L. Sun, Q. Lei, B. Peng, G.M. Kontogeorgis, X. Liang, An analysis of the parameters in the Debye-Hückel theory, Fluid Phase Equilib., 556 (2022) 113398, doi: 10.1016/j.fluid.2022.113398.
[41] A. Jacob, M. Peltz, S. Hale, F. Enzmann, O. Moravcova, L.N. Warr, G. Grathoff, P. Blum, M. Kersten, Simulating permeability reduction by clay mineral nanopores in a tight sandstone by combining computer X-ray microtomography and focussed ion beam scanning electron microscopy imaging, Solid Earth, 12 (2021) 1–14.
[42] S.S. Patil, M.T. Dissertation, Voxel-Based Solid Models: Representation, Display and Geometric Analysis, Indian Institute of Technology, Bombay, 2005.
[43] P. Suchde, T. Jacquemin, O. Davydov, Point cloud generation for meshfree methods: an overview, Arch. Comput. Methods Eng., 30 (2023) 889–915.
[44] C. Newtonian, I. Newtonian, T. Navier, T. Navier, Derivation of the Navier–Stokes Equations, 2015, pp. 1–8.
[45] A.J. Chorin, A numerical method for solving incompressible viscous flow problems, J. Comput. Phys., 2 (1967) 12–26.
[46] V.-T. Nguyen, W.-G. Park, A review of preconditioning and artificial compressibility dual-time Navier–Stokes solvers for multiphase flows, Fluids, 8 (2023) 100, doi: 10.3390/fluids8030100.
[47] L.M. Anovitz, D.R. Cole, Characterization and analysis of porosity and pore structures, Rev. Mineral. Geochem., 80 (2015) 61–164.

[48] S. Gaboreau, J.C. Robinet, D. Prêt, Optimization of pore-network characterization of a compacted clay material by TEM and FIB/SEM imaging, Microporous Mesoporous Mater., 224 (2016) 116–128.
[49] P.-E. Øren, S. Bakke, Process based reconstruction of sandstones and prediction of transport properties, Transp. Porous Media, 46 (2002) 311–343.
[50] C.A. Schneider, W.S. Rasband, K.W. Eliceiri, NIH Image to ImageJ: 25 years of image analysis, Nat. Methods, 9 (2012) 671–675.
[51] L.M. Keller, P. Schuetz, R. Erni, M.D. Rossell, F. Lucas, P. Gasser, L. Holzer, Characterization of multi-scale microstructural features in opalinus clay, Microporous Mesoporous Mater., 170 (2013) 83–94.
[52] C. Chen, D. Hu, D. Westacott, D. Loveless, Nanometer-scale characterization of microscopic pores in shale kerogen by image analysis and pore-scale modeling, Geochem. Geophys. Geosyst., 14 (2013) 4066–4075.
[53] R. Wakeman, The influence of particle properties on filtration, Sep. Purif. Technol., 58 (2007) 234–241.
[54] E. Escalera, M.L. Antti, M. Odén, Thermal treatment and phase formation in kaolinite and illite based clays from tropical regions of Bolivia, IOP Conf. Ser.: Mater. Sci. Eng., 31 (2012) 012017, doi: 10.1088/1757-899X/31/1/012017.
[55] FAO, Standard Operating Procedure for Cation Exchange Capacity and Exchangeable Bases, The Food and Agriculture Organization of the United Nations, 2022.
[56] D. Jaremko, D. Kalembasa, A comparison of methods for the determination of cation exchange capacity of soils, Ecol. Chem. Eng. S, 21 (2014) 487–498.
[57] V.A. Nguyen, M. Ramanathan, Application of Brunauer–Emmett–Teller (BET) theory and the Guggenheim–Anderson–de Boer (GAB) equation for concentration-dependent, non-saturable cell–cell interaction dose-responses, J. Pharmacokinet. Pharmacodyn., 47 (2020) 561–572.
[58] A. Tironi, M.A. Trezza, E.F. Irassar, A.N. Scian, Thermal treatment of kaolin: effect on the pozzolanic activity, Procedia Mater. Sci., 1 (2012) 343–350.
[59] W.F. Woodruff, A. Revil, CEC-normalized clay-water sorption isotherm, Water Resour. Res., 47 (2011) 1–15, doi: 10.1029/2011WR010919.
[60] BIS, Indian Standard Drinking Water Specification (Second Revision), Bureau of Indian Standards, IS 10500, 2012, pp. 1–11.
[61] W. Wang, A.N. Kravchenko, A.J.M. Smucker, M.L. Rivers, Comparison of image segmentation methods in simulated 2D and 3D microtomographic images of soil aggregates, Geoderma, 162 (2011) 231–241.